Singular angular magnetoresistance and sharp resonant features in a high-mobility metal with open orbits, math xmlns="http://www.w3.org/1998/Math/MathML">mrow>msub>mi>ReO/mi>mn>3/mn>/msub>/mrow>/math>

Nicholas P. Quirk, Loi T. Nguyen, Jiayi Hu, R. J. Cava, and N. P. Ong

Phys. Rev. Materials **5**, 105004 — Published 27 October 2021

DOI: 10.1103/PhysRevMaterials.5.105004

Singular angular magnetoresistance and sharp resonant features in a high-mobility metal with open orbits, ReO_3

Nicholas P. Quirk[1], Loi T. Nguyen[2], Jiayi Hu[1], R. J. Cava[2], N. P. Ong[1]
Department of Physics[1] *and Department of Chemistry*[2]*, Princeton University, Princeton, NJ 08544*

We report high-resolution angular magnetoresistance (AMR) experiments performed on crystals of ReO_3 with high mobility (>100,000 cm^2/Vs at 2 K) and extremely low residual resistivity (5-8 nΩcm). The Fermi surface, comprised of intersecting cylinders, supports open orbits. The resistivity ρ_{xx} in a magnetic field $B = 9$ T displays a singular pattern of behavior. With $\mathbf{E} \parallel \hat{\mathbf{x}}$ and $\mathbf{B}$ initially $\parallel \hat{\mathbf{z}}$, tilting $\mathbf{B}$ in the longitudinal k_z-k_x plane leads to a steep decrease in ρ_{xx} by a factor of 40. However, if $\mathbf{B}$ is tilted in the transverse k_y-k_z plane, ρ_{xx} increases steeply by a factor of 8. Using the Shockley-Chambers tube integral approach, we show that, in ReO_3, the singular behavior results from the rapid conversion of closed to open orbits, resulting in opposite signs for AMR in orthogonal planes. The floor values of ρ_{xx} in both AMR scans are identified with specific sets of open and closed orbits. Also, the "completion angle" γ_c detected in the AMR is shown to be an intrinsic geometric feature that provides a new way to measure the Fermi radius k_F. However, additional sharp resonant features which appear at very small tilt angles in the longitudinal AMR scans are not explained by the tube integral approach.

I. INTRODUCTION

The past decade has witnessed renewed interest in semimetals and metals that exhibit unusually high carrier mobilities. In the Dirac semimetal Cd_3As_2, the mobility μ can attain 10^7 cm^2/Vs [1]. The large-μ semimetal WTe_2 displays non-saturating magnetoresistance in magnetic fields up to 60 T [2]. The Weyl semimetals TaAs, NbAs and NbP have mobilities exceeding 150,000 cm^2/Vs. These enhanced μ may result from a very small effective mass in the vicinity of avoided band crossings and protection from carrier scattering. In metals, the Fermi energy is remote from such band crossings, but high-mobility candidates have also been identified, e.g. $PdCoO_2$, $PtCoO_2$ [3–6] and Pd_3Pb [7]. For Fermi surfaces that are mutliply connected, angular magnetoresistance (AMR) is a powerful tool for unravelling how connectivity affects transport. Although AMR is most frequently employed to map the angular variation of the Shubnikov de Haas (SdH) period, for e.g., in Sr_2RuO_4 [8] and the Bechgaard salts, it can also uncover surprising features unrelated to SdH oscillations. The Yamaji angle detected in the Bechgaard salts is a well-known example [9, 10]. A more recent example is the existence of ultra-narrow peaks in the AMR of the magnetic Weyl semimetal CeAlGe when $\mathbf{B}$ is aligned with symmetry axes [11].

Here we report novel features observed in the AMR of crystals of ReO_3 that exhibit extremely low residual resistivities. ReO_3 is the archetypal example of a metal in which the Fermi surface (FS) forms a three-dimensional (3D) jungle-gym network of intersecting cylinders plus two small closed surfaces [12–14]. Early experiments on ReO_3 are reported in Refs. [15–19]. A recent angle-resolved photoemission experiment obtains close agreement of the observed Fermi surface with *ab initio* calculations employing WIEN2K within the generalized gradient approximation (GGA) [20]. From a modern viewpoint, ReO_3 has some interesting features. The lattice structure, comprised of a Re ion surrounded by six nearest neighbor O ions, is the simplest expression of a 3D Lieb lattice [21]. A hallmark of Lieb lattices is the existence of flat bands caused by wave-function interference [22, 23]. In ReO_3, flat bands are prominent along X-M, but they lie too far from the Fermi level (by 1 eV) to affect transport directly.

We have grown crystals in which the residual resistivity ρ_{00} is 5 to 8 nΩcm at 2 K (comparable to that in $PdCoO_2$ [3] and 6-10 times lower than in ultra-pure Au). At 2 K, μ is estimated to be >100,000 cm^2/Vs. This corresponds to a transport mean free path of 25 μm. In these crystals we have uncovered a singular feature in the AMR. With axes x, y and z fixed parallel to the cylinders' axes, and the electric field $\mathbf{E} \parallel \hat{\mathbf{x}}$ (Fig. 1), we observe the longitudinal resistivity ρ_{xx} to decrease by a factor of $\sim$40 when $\mathbf{B}$ (fixed at 9 T) is tilted towards $\mathbf{E}$. However, if $\mathbf{B}$ is tilted in the plane orthogonal to $\mathbf{E}$, ρ_{xx} exhibits a 10-fold increase. The extreme anisotropy in the response of ρ to slight angular deviations from the singular point $(\theta, \chi) = (0, 0)$ ($\mathbf{B} \parallel \hat{\mathbf{z}}$) has not been reported previously in any metal to our knowledge. All the AMR curves investigated (as well as the Hall response) display a sharp discontinuity at a characteristic angle $\gamma_c \simeq 29°$. Moreover, we observe weak features in the scans vs. θ (sharp resonances) suggestive of enhanced scattering at specific tilt angles 1.1° and 2.2°.

We describe a semiclassical model based on open orbits on the jungle-gym Fermi surface (FS) that emphasizes the connectivity of the orbits in tilted $\mathbf{B}$ and the key role of orbital links that convert closed to open orbits. The model accounts for the opposite signs of the AMR vs. θ and χ, as well as the physical meaning of γ_c which we call the "completion" angle. However, it is inadequate for explaining the cusp-like sensitivity at very small tilt angles or the appearance of sharp resonances.

II. EXPERIMENTAL RESULTS

Crystals of ReO_3 were grown by double-pass chemical vapor transport. A silica tube of inner diameter 14 mm and length 30 cm was loaded with 1 g of ReO_3 powder and 25 mg of iodine flakes and sealed under vacuum. The tube was inserted into a 3-zone horizontal tube furnace in which the temperature was slowly raised over 6 h to 500°C (hot end) and 450°C (cool end). After 4 days of vapor transport, the furnace was cooled over 10 h to 290 K. Vapor transport, again using iodine, was then repeated to enhance the crystal purity. Large, red, plate-like crystals up to 1 cm on a side were harvested at the cold end (Fig. 1a). The phase purity and crystal structure of ground crystals were determined by powder x-ray diffraction using a Bruker D8 Advance Eco with Cu K radiation and a LynxEye-XE detector. The cubic cell parameter a is 3.748 Å.

Figure 1b shows a sketch of the jungle gym FS, using the value of the Fermi radius $k_F = 0.386$ Å^{-1} derived from Refs. [15–17]. In the profile of the zero-B resistivity ρ vs. T (Fig. 1c), ρ maintains its ultra-low residual value ρ_{00} (inset) to an unusually high $T \sim 20$ K, implying that phonon scattering is suppressed until T exceeds ~ 20 K. The residual resistivity ratio $\rho(300\,\mathrm{K})/\rho_{00}$ is 1,500. The T-dependent part $\Delta\rho(T) = \rho(T) - \rho_{00}$ fits well to T^η up to 80 K (Fig. 1d) with an exponent $\eta \simeq 3.1 \pm 0.2$, much reduced from that in the Bloch law (T^3 vs. T^5). See the case of $PdCoO_2$ [3] as well.

We selected crystals with optimal rectangular shape (1.0×0.5 mm^2 in area) and mechanically polished the broad faces with fine sandpaper to reduce the thicknesses to 80-100 µm. The edges of the broad face are aligned (to a precision of ±1°) with k_x and k_y of the lattice. In all field-tilt measurements, we define the x, y, and z axes to be anchored to the k_x, k_y and k_z axes of the lattice, respectively (Fig. 1b). Both the electric field $\mathbf{E}$ and the (spatially averaged) current density $\langle \mathbf{J} \rangle$ are $\parallel \hat{\mathbf{x}}$. The contact resistances of the Ag paint contacts were under 2 Ω.

We estimated the carrier mobility ($\approx 10^5$ cm^2/Vs at 2 K) by measuring the field dependence of the resistivity tensor up to 9 T at zero tilt angle and inverting it to produce σ_{xx}(B) and σ_{xy}(B). The average carrier mobility may be estimated by the inverse of the field at which σ_{xy}(B) exhibits a sharp peak (Fig. S3). In two samples, this value was 0.16 T (corresponding to a mobility of 60,000 cm^2/Vs) and 0.08 T (125,000 cm^2/Vs). In section III, we use the zero-field conductivity ($1/\rho_{00}$) and the Fermi surface dimensions reported by Refs. [15–19] to calculate the electron mobility as $\mu = 90{,}000$ cm^2/Vs.

The sample platform was tilted using a horizontal rotator in a Quantum Design PPMS equipped with a 9-Tesla magnet. The field tilt angles, θ and χ defined in Fig. 1b were measured with a transverse Hall sensor (Lakeshore HGT 2101-10) to a resolution of ±0.03°. The 4-probe measurements of resistances were performed using a Keithley 6221 DC current source and 2182a nanovoltmeter in Delta mode using current pulses of 5-10 mA.

When $\mathbf{B}$ is tilted by θ in the longitudinal x-z plane with χ fixed at 0, $\rho_{xx}(\theta, 0)$ displays sharp maxima at $\theta = 0$ and 180°. Figure 2a plots $\rho_{xx}(\theta, 0)$ vs. θ measured at $T = 1.9$ K (red curve). We call this the longitudinal AMR (LAMR) curve. In the polar plot, the LAMR curve describes two very narrow plumes directed along $\theta = 0$ and 180° (red curves in Fig. 2b). An expanded view of the LAMR curve is shown in semilog scale in Fig. 2c. As θ increases from 0, ρ_{xx} decreases steeply by a factor of ~ 40 (semilog plot in Fig. 2c). A characteristic angle $\gamma_c \sim 29°$ (which we call the "completion" angle) is prominently seen in all AMR curves investigated. In the LAMR scan, $\rho_{xx}(\theta, 0)$ displays a rounded step-drop to the "floor" value $\rho^{L,fl}$, where it remains until $\theta \to 150°$. We have $\rho^{L,fl} \simeq 20 \times \rho_{00}$.

The transverse AMR (TAMR) curve plotting $\rho_{xx}(0, \chi)$ vs. χ with $\mathbf{B}$ lying in the transverse y-z plane, are radically different (blue curve in Fig. 2a). At small tilt angle ($|\chi| < 15°$), ρ_{xx} increases steeply to a peak value 8-10× higher than at $\chi = 0$. Further increase of χ to γ_c leads to a steep decrease to a resistivity floor value $\rho^{T,fl}$ that is 10× larger than the floor value $\rho^{L,fl}$ in the LAMR (see the semilog plot in Fig. 2c). We estimate $\rho^{T,fl} = 4.5 \times \rho^{L,fl} \gg \rho_{00}$. The polar plot of the TAMR curve (blue curve in Fig. 2b) shows an 8-petal floral pattern with C_4 symmetry weakly broken by misalignment.

In principle, the sharp maximum in ρ_{xx} at $\theta = 0$ in the LAMR curve must equal the minimum in the TAMR at $\chi = 0$. In our experiment, however, a residual misalignment leads to a difference of a factor of 4. The singular behavior in the vicinity of $(\theta, \chi) = (0, 0)$ amplifies errors caused by angular misalignments of ±1° (the difficulty is roughly similar to aligning the tips of two sharp needles). The traces in Fig. 2 result from progressive alignment improvements in repeated scans. The misalignment also accounts for slight deviations from C_4 symmetry in the polar plot of the TAMR curve.

Returning to the LAMR curve, we resolve weak, ultra-narrow resonant features at small θ. The expanded view in Fig. 2d displays three LAMR scans measured at 1.9 K with $|\mathbf{B}|$ fixed at 6, 7.5 and 9 T. In each curve, ρ_{xx} displays distinct peaks with ultra-narrow widths ($\sim 0.1°$) centered at $\theta = 0$, ±1.1° and ±2.2°. The peak amplitudes are strongest at 0° and ±2.2°. Because their angular positions are independent of B, they are unrelated to quantization of the magnetic flux. We discuss their origin below.

To complement the longitudinal resistivity, we have also performed Hall measurements. In Fig. 3a, the green curve plots the angular Hall resistivity $\rho_{yx}(\theta, 0)$ vs. θ in the LAMR experiment (ρ_{yx} depends on $B\cos\theta$ so it is even in θ). At the angle γ_c, ρ_{yx} displays a remarkable step-decrease that involves a sign change. Inverting the resistivity matrix $\rho_{ij}(\theta, 0)$, we obtain the conductivity matrix $\sigma_{ij}(\theta, 0)$. The curves of σ_{xx} (red) and σ_{xy} (green) are plotted in Fig. 3b. As θ increases from 0, the conductivity $\sigma_{xx}(\theta, 0)$ increases monotonically up to

γ_c, above which it becomes nearly independent of θ. The more interesting Hall curve $\sigma_{xy}(\theta, 0)$ is initially negative at $\theta = 0$. It displays a broad minimum near 12° and then increases steeply to positive values above 16°. At γ_c, however, σ_{xy} suffers a giant discontinuity, ending back at a large negative value that slowly increases in magnitude as $\theta \to 45°$.

In our analysis (next section), we have focused on understanding the diagonal conductivity element σ_{xx}. The Hall conductivity σ_{xy} is more difficult to analyze because the competing hole-like and electron-like contributions demand better estimates of the Hall currents. The interesting Hall behavior is deferred for further investigation.

III. SEMICLASSICAL MODEL

Given the $\mathcal{C}_4$ symmetry of the lattice, the sign difference of the AMR scans vs. θ and χ and their steep variations are unexpected at first glance. We show that the Shockley-Chambers tube-integral approach [24] can account qualitatively for the sign difference and floor values observed. Although AMR curves are usually difficult to calculate, there are several mitigating factors in this material. *Ab initio* calculations [12–14] reveal that the cylinders have uniform cross-sections which simplifies the evaluation of the tube integral. Moreover, the condition $\mu B \gg 1$ ensures that the cylinders dominate the conductivity matrix element σ_{xx}. (As discussed later, the sharp "resonant" features appearing in LAMR seem to require a more sophisticated treatment.)

In a magnetic field, σ_{ab} is given by the Shockley-Chambers tube integral (see Appendix)

$$\sigma_{ab} = \frac{2e^2}{(2\pi)^3\hbar^2}\int \frac{m^*}{\omega_c}\mathcal{C}_{ab}\, dk_H, \qquad (1)$$

with the velocity-velocity correlator $\mathcal{C}_{ab}$ given by

$$\mathcal{C}_{ab} = \left(\frac{\hbar k_F}{m_0}\right)^2 \frac{1}{(1-e^{-2\pi\alpha})} \times \int_0^{2\pi} d\phi \int_0^{2\pi} d\phi'\; v_a(\phi) v_b(\phi - \phi')\; e^{-\alpha\phi'}. \qquad (2)$$

where $\mathbf{v}(\mathbf{k})$ is the group velocity, m_0 the band mass, and $\alpha = (\omega_c\tau)^{-1}$.

We approximate the FS as three intersecting cylinders (radius k_F), C_x, C_y and C_z, with axes along $\hat{\mathbf{x}}$, $\hat{\mathbf{y}}$ and $\hat{\mathbf{z}}$, respectively (Fig. 4a).

We assume $\mathbf{E} \parallel \hat{\mathbf{x}}$ throughout. It is convenient to denote the conductivity of an isolated cylinder in zero B as

$$\sigma_0^{(1)} = n^{(1)} e\mu, \qquad (3)$$

where $n^{(1)}$, the carrier density enclosed within the cylinder, is given by

$$n^{(1)} = 2\frac{\pi k_F^2}{(2\pi)^3}(K - 2k_F), \qquad (4)$$

where k_F is the radius of the cylinder, $K = 2\pi/a$ and a is the primitive lattice spacing. In a tilted $\mathbf{B}$, Eq. 16 in the Appendix gives for C_y (in isolation) the conductivity $\sigma_{xx}^{Cy} = \sigma_0^{(1)}/(1 + (\mu B_y)^2)$.

Including both C_y and C_z, the measured residual resistivity at $B = 0$ is then $1/\rho_{00} = 2n^{(1)}e\mu$. With $K \simeq 4k_F$, we find $n^{(1)} \simeq 0.75 \times 10^{22}$ cm^{-3}, which yields $\mu = 90{,}000$ cm^2/Vs. This estimate agrees with the low-field peak in the Hall conductivity σ_{xy}, which occurs at $B = 0.08$ T at 2 K (Fig. S3). The inferred transport mean free path is then $l_{mfp} = \hbar k_F \mu/e = 25$ μm.

We next consider open orbits. In a tilted $\mathbf{B}$, a wave packet on the FS moves along an orbit (red curves in Fig. 4a) defined by the intersection of a plane normal to $\mathbf{B}$ (pale blue plane) and the FS. As drawn, the right-moving wave packet on cylinder C_y, loops under C_x (dashed curve) before resuming its straight-line path on C_y, whereas the left-moving wave packet in the companion orbit loops over C_x. In the high-field limit, such open orbits, with non-vanishing v_x, dominate the conductivity σ_{xx}.

With $\mathbf{B}$ strictly $\parallel \hat{\mathbf{z}}$, the orbits on the cylinder C_z are closed and electron-like. The orbits on cylinders C_x and C_y are also closed (apart from a negligible subset at the top and bottom of C_x and C_y for which $v_x = 0$). However, they are hole-like (comprised of alternating straight segments on C_x and C_y). Because of the high mobility, the contributions of the closed hole orbits on cylinders C_x and C_y to σ_{xx} decrease as $1/B^2$ when $\mu B \gg 1$. The absence of open orbits causes the resistivity to increase monotonically in the large-B regime, as observed. Our analysis focuses on the conversion of closed to open orbits for states on C_x and C_y. The cylinder C_z is less important for the AMR. However, it plays the dominant role in the angular Hall conductivity $\sigma_{xy}(\theta, 0)$ (Fig. 3b), which we leave for a future study.

A. LAMR

In the LAMR experiment, we observe a dramatic increase in σ_{xx} when $\mathbf{B}$ is tilted, even slightly, in the longitudinal k_x-k_z plane. To show that this results from a sharp increase in the fraction of open-orbit states, we consider the set of planes normal to $\mathbf{B}$. Figure 4b shows cross-sections of three C_y cylinders separated by $K = 2\pi/a$ in the repeated zone scheme, together with two planes at the tilt angle θ. The planes that are tangential to the outer cylinders (blue lines) intersect the middle cylinder to define two FS arcs hosting open-orbit states (thick green arcs in Fig. 4b). A wavepacket prepared initially on the left green arc on C_y loops under C_x (as a "looped segment") then alternates between straight-line segments on C_y and looped segments on C_x (thick red curves in Fig. 4a). Conversely, if the initial state lies outside the green arcs, the wavepacket runs into a neighboring C_y before it can complete a loop on C_x. These states, lying in the "shadow" cast by adjacent cylinders, remain trapped in closed hole-like orbits.

The looped segments on C_x are crucial for linking straight segments on C_y into open orbits even though they themselves do not contribute to σ_{xx}. Increasing θ converts more of the states on C_x to looped segments (as the fraction in the shadow decreases). This results in a sharp increase in the fraction of states on C_y that become open orbits. Hence σ_{xx} increases rapidly with θ.

B. Completion Angle

The increase in σ_{xx} ends abruptly when the blue line becomes the inner tangent to adjacent cylinders (red dashed line in Fig. 4b) at the "completion angle" γ_c given by

$$\sin\gamma_c = \frac{2k_F}{K}. \tag{5}$$

The completion angle provides a direct way to measure k_F.

As mentioned, ρ_{xx} abruptly drops to its "floor" value at $\gamma_c \sim 29°$ and stays there until θ exceeds 150° (Fig. 2c). Using Eq. 5, we find that $k_F/K = 0.25$, in good agreement with de-Haas-van Alphen experiments [15–17] which reported $k_F/K = 0.23$. The negative LAMR profile provides a new way to measure k_F in ReO_3. In both the Hall scan and the TAMR experiment, the step-changes at γ_c are much more pronounced.

In the floor interval $\gamma_c < \theta < \pi - \gamma_c$, nearly all the states on C_y belong to open orbits (the green arcs in Fig. 4b cover the entire cross section). As noted in the Appendix (line below Eq. 16), $\mathbf{B}$ has no effect on open orbits. Hence the conductivity contribution from C_y reverts to its zero-B value $\sigma_0^{(1)}$. In the same interval $\gamma_c < \theta < \pi - \gamma_c$, all the states on C_z execute closed cyclotron orbits driven by the field component $B_z = B\cos\theta$. By Eq. 16, the conductivity contribution from C_z is then $\sigma_0^{(1)}/(1 + (\mu B\cos\theta)^2)$. As a result, the total conductivity in the floor interval is

$$\sigma^{L,fl} = \sigma_0^{(1)}\left[1 + \frac{1}{1 + (\mu B\cos\theta)^2}\right]. \tag{6}$$

This conclusion is in accord with our experiment. Although ρ_{xx} in the floor interval is indeed very low (red curve for $|\theta| > 30°$ in Fig. 2a), it is still nearly twice the residual resistivity (measured in zero B) $\rho_{00} = 1/(2\sigma_0^{(1)})$.

C. TAMR

We turn next to the TAMR experiment with $\mathbf{B}$ tilted in the plane k_y-k_z transverse to $\mathbf{E}$ (Fig. 4c). Now, the conversion of states on C_y into looped segments directly suppresses their conductivity. Initially, with $\chi = 0$ ($\mathbf{B} \parallel \hat{\mathbf{z}}$), the states $\mathbf{k}$ on C_y contribute strongly to σ_{xx} despite being parts of hole-type closed orbits. At finite χ, a subset of the planes normal to $\mathbf{B}$ intersect C_y to define the surface of a conical wedge (inset in Fig. 4c). As discussed above, the orbits covering the wedge are looped segments that link straight segments on C_x to form open orbits. At the extrema of the loop, the x-component of $\mathbf{v}(\mathbf{k})$ vanishes. Since $\mathbf{v}$ appears squared in $\mathcal{C}_{ab}$ (Eq. 2), this results in a strong suppression of the conductance. In effect, a finite χ converts high-conductance states on C_y to ones with vanishing conductivity. With increasing χ, the conversion proceeds until it consumes all the high-conduction states on C_y. This occurs at the completion angle $\gamma_c \sim 29°$ (Eq. 5).

Using the tube integral, we have calculated the suppression of σ_{xx} in the wedge as a function of χ. For the cylinder C_y, the elliptical orbit on the tilted plane can be projected onto a circular orbit $\mathcal{P}$ in the cross-section of the cylinder (inset in Fig. 4c). On $\mathcal{P}$, the phase variable ϕ then becomes just the azimuthal angle φ, which greatly simplifies the calculation of $\mathcal{C}_{ab}$.

As a wavepacket traverses a looped segment, its orbit projects onto an arc of angular length 2β on $\mathcal{P}$. As shown, the angular half-length β_0 of the longest loop segment is given by

$$1 - \cos\beta_0 = \left(\frac{K}{k_F} - 1\right)\tan\chi. \tag{7}$$

We have integrated $0 < \beta < \beta_0$ numerically to determine the value of the conductivity σ_{loop} at each χ (Fig. S1). The maximum net conductivity from C_y (attained when $\chi = \gamma_c$) is under 0.5% of that at $\chi = 0$.

Finally, once χ exceeds γ_c, the states on C_y abruptly disconnect from open orbits to execute closed cyclotron orbits driven by the field component $B_y = B\sin\chi$. By contrast, the closed orbits in C_z are driven by the complementary component $B_z = B\cos\chi$. With all states in C_y and C_z in closed orbits (Eq. 16), the total conductivity in the interval $\gamma_c < \chi < \pi/2 - \gamma_c$ is

$$\sigma^{T,fl} = \sigma_0^{(1)}\left[\frac{1}{1 + (\mu B\sin\chi)^2} + \frac{1}{1 + (\mu B\cos\chi)^2}\right]. \tag{8}$$

As $\sigma^{T,fl} \ll \sigma^{L,fl}$, Eq. 8 implies that the observed resistivity within this interval (blue curve in Fig. 1a in interval $29° < \chi < 65°$) is much larger than the floor value in the LAMR scan (red curve), again in agreement with experiment.

This holds until χ increases beyond $\pi/2 - \gamma_c$. Then the looped segments wrap around C_z instead of C_x, and ρ_{xx} rises steeply.

In both LAMR and TAMR scans, these large-angle features are qualitatively consistent with the experiment. A quantitative comparison with ρ_{xx} requires a more involved calculation of σ_{xy} (which can be larger than σ_{xx}).

IV. SHARP RESONANT FEATURES

To investigate the highly unusual LAMR behavior in the limit of small tilt angles, we have performed high-resolution measurements of ρ_{xx} vs. θ at fixed B. As shown in Fig. 3c, the profile of ρ_{xx} vs. θ displays a sharp cusp in the limit $\theta \to 0$. This implies that ρ_{xx} deviates from its value at $(0,0)$ in a non-analytical way. More interestingly, we observe weak peaks at $\theta = 1.1^\circ$ and 2.2°. Above the angle 2.2°, ρ_{xx} steepens its decrease with θ, displaying a sharp break in slope. Because the angular positions of the resonances are independent of B, they are unrelated to Landau quantization effects. The tiny B-independent angles suggest to us that the features are geometric in origin, arising resonantly at small θ from very large orbits that extend over multiple Brillouin zones.

A conceptual difficulty in analyzing the small tilt regime is the appearance of quasiperiodic orbits. In Fig. S2 (Appendix), we plot numerical simulations of the combination of closed and open orbits that appear at small tilt angles $\theta = 1^\circ, 5^\circ$ and 10° in the LAMR experiment. In each panel, the plot extends over 25 Brillouin Zones. The orbits are subtly quasiperiodic despite the nominal repetition. As it stands, the tube-integral approach lacks the formalism to handle quasiperiodic orbit patterns.

V. CONCLUSION

High-resolution angular magnetoresistance performed in the regime $\mu B \gg 1$ in high-mobility metals can uncover novel features that are not evident in conventional Shubnikov de Haas oscillations. In ReO_3 with $\mu \sim 90{,}000$ cm^2/Vs, we observe a singular variation of the resistivity: ρ_{xx} decreases steeply by a factor of 40 when $\mathbf{B}$ is tilted in the longitudinal plane containing $\mathbf{E}$. However, it rises steeply by a factor of 8-10 when $\mathbf{B}$ is tilted in the plane orthogonal to $\mathbf{E}$. Using the tube integral approach, we show that this previously unreported singular variation is inherent to the jungle-gym FS geometry. The AMR profiles display a rounded shoulder at a completion angle γ_c that is an intrinsic feature of the FS topology. In addition to explaining γ_c, the tube-integral approach accounts for the relative magnitudes of the floor values in both the LAMR and TAMR scans. However, the semiclassical model fails to explain the series of sharp resonant features observed in the LAMR scans (or the cuspy variations as θ and χ approach zero). These features, which may involve orbit patterns extending over multiple Brillouin zones, invite further investigation.

* * *

Appendix: Shockley-Chambers tube integral

In general, the semiclassical conductivity in a strong magnetic field $\mathbf{B}$ can be computed using the Shockley-Chambers tube integral [10, 24]

$$\sigma_{ab} = \frac{2e^2}{(2\pi)^3\hbar^2}\int \frac{m^*}{\omega_c}\mathcal{C}_{ab}\, dk_H, \tag{9}$$

where $\mathcal{C}_{ab}$ is the velocity-velocity correlator discussed below. The states in $\mathbf{k}$ space are divided into a set of parallel planes normal to $\hat{\mathbf{n}}$ and indexed by $k_H = \mathbf{k}\cdot\hat{\mathbf{n}}$, where $\hat{\mathbf{n}} = \mathbf{B}/|\mathbf{B}|$. In Eq. 9, ω_c is the angular frequency of a cyclotron orbit confined to a plane with m^* the cyclotron mass. We may express m^* as the derivative with respect to the energy ε of the area $\mathcal{A}$ enclosed by the cyclotron orbit, i.e.

$$m^* = \frac{\hbar^2}{2\pi}\frac{\partial\mathcal{A}}{\partial\varepsilon}. \tag{10}$$

The velocity-velocity correlator $\mathcal{C}_{ab}$ is given by

$$\mathcal{C}_{ab} = \int_0^{2\pi} d\phi \int_0^{\infty} d\phi' v_a(\phi)v_b(\phi-\phi')\, e^{-\alpha\phi'}. \tag{11}$$

Here $\mathbf{v}(\phi)$ is the group velocity at the phase coordinate $\phi = (\omega_c/eB)\int^{\mathbf{k}} dk/v_\perp$ in a cyclotron orbit, with $v_\perp = |\mathbf{v}\times\hat{\mathbf{n}}|$.

Equation 9 is derived using the Green's function of the high-B Boltzmann equation [24]. The contribution to σ_{ab} of a state at the phase coordinate ϕ is the sum of wave packets created with velocity v_b by a train of E-field δ-function pulses applied at all earlier times corresponding to the phase coordinate $\phi - \phi'$. The wave packets advance along the cyclotron trajectory at the rate $\dot{\phi}' = \omega_c$ while decaying exponentially with the decay constant $\alpha = (\omega_c\tau)^{-1}$ where τ is the lifetime.

By segmenting the interval $0 < \phi' < \infty$ into finite segments, we simplify $\mathcal{C}_{ab}$ to

$$\mathcal{C}_{ab} = \left(\frac{\hbar k_F}{m_0}\right)^2 \frac{1}{(1-e^{-2\pi\alpha})} \times \int_0^{2\pi} d\phi \int_0^{2\pi} d\phi'\, v_a(\phi)v_b(\phi-\phi')\, e^{-\alpha\phi'}. \tag{12}$$

Our goal is to find σ_{xx} of the cylinder C_y in a field $\mathbf{B}$ tilted at angle $\pi/2-\chi$ to its axis. If we assume the quadratic dispersion $\varepsilon(\mathbf{k}) = \hbar^2(k_x^2+k_y^2)/2m_0$ with band mass m_0, Eq. 10 gives

$$m^* = m_0/\sin\chi, \quad \alpha = (\omega_c\tau)^{-1} = (\mu|\mathbf{B}|\sin\chi)^{-1}. \tag{13}$$

With $\mu \simeq 90{,}000$ cm^2/Vs, we have $\mu B \simeq 81$ at 9 T.

For the cylinder, the cyclotron period in tilted $\mathbf{B}$ is identical to that of a circular orbit $\mathcal{P}$ projected onto the cross-section in the k_x-k_z plane and driven by the field component along $\hat{\mathbf{y}}$, $B_y = B\sin\chi$ (inset, Fig. 4c). Moreover, we can replace the phase variable ϕ with the azimuthal angle φ in $\mathcal{P}$ (inset in Fig. 4c). The cylindrical geometry enables each $\mathbf{k}$ and its velocity $\mathbf{v}(\mathbf{k})$ to be mapped one-to-one to corresponding vectors on $\mathcal{P}$. The mapping greatly simplifies the calculation of σ_{xx}.

Isolated cylinder

We first consider an isolated cylinder with axis $\parallel \hat{\mathbf{y}}$ in a field $\mathbf{B}$ tilted at an angle χ to $\hat{\mathbf{z}}$ in the y-z plane ($\mathbf{E} \parallel \hat{\mathbf{x}}$). The cylinder accommodates an electron density

$$n_\ell = \frac{2}{(2\pi)^3}\pi k_F^2 K_\ell, \tag{14}$$

where K_ℓ is its length. The orbits are closed ellipses with m^* and α given by Eq. 13. Integrating φ and φ' over $(0, 2\pi)$ in Eq. 12 gives for both $\mathcal{C}_{xx}$ and $\mathcal{C}_{zx}$:

$$\mathcal{C}_{xx} = \left(\frac{\hbar k_F}{m_0}\right)^2 \frac{\pi\alpha}{1+\alpha^2}, \quad \mathcal{C}_{zx} = \left(\frac{\hbar k_F}{m_0}\right)^2 \frac{\pi}{1+\alpha^2} \tag{15}$$

Using these expressions in Eq. 9, the conductivity σ_{xx} and the Hall conductivity σ_{xy} are

$$\sigma_{xx} = \frac{n_\ell e\mu}{[1+(\mu B\sin\chi)^2]}, \quad \sigma_{zx} = \frac{n_\ell e\mu^2 B\sin\chi}{[1+(\mu B\sin\chi)^2]}, \tag{16}$$

where $\mu = e\tau/m_0$ is the mobility.

In the limit $\chi \to 0$ ($\mathbf{B} \perp$ axis), σ_{xx} recovers its zero-B value $n_\ell e\mu$. This is the simplest example of an open-orbit conductivity that is B-independent even when $\mu B \gg 1$.

Jungle gym FS

Next, we apply the tube integral to address the TAMR experiment in the jungle-gym FS with intersecting cylinders (Fig. 4c). Tilting of $\mathbf{B}$ in the k_x-k_z plane causes a fraction of the hole-like closed orbits to become looped segments that belong to open orbits. The loops are shown as red curves on the curved area of the conical wedge shown in white in inset of Fig. 4c. In the open orbit, the wave packets traverse alternatingly straight segments on C_x and looped segments on C_y until they damp out.

As $v_x = 0$ on the former, only the looped segments contribute to σ_{xx}. Projecting the loop to the circular orbit $\mathcal{P}$ on the cross-section (inset in Fig. 4c), the azimuthal angle φ on $\mathcal{P}$ runs from $\pi/2-\beta$ to $\pi/2+\beta$ to describe an arc of angular length 2β. Since the planes are indexed by k_H, $d\beta$ and dk_H are related by

$$dk_H = k_F\cos\chi\sin\beta d\beta. \tag{17}$$

Evaluating the integrals over φ and φ' in $\mathcal{C}_{xx}$ between the limits $(\pi/2-\beta,\, \pi/2+\beta)$, we have

$$\mathcal{C}_{xx}(\beta) = \left(\frac{\hbar k_F}{m_0}\right)^2 \frac{1}{(1-e^{-2\pi\alpha})}\frac{2e^{-\alpha\pi/2}}{(1+\alpha^2)}(\beta - \frac{1}{2}\sin 2\beta)\times \\ [\alpha\sin\beta\cosh\alpha\beta - \cos\beta\sinh\alpha\beta]\,. \tag{18}$$

As mentioned, the looped segments cover the curved area of the conical wedge (inset of Fig. 4c). The longest orbit, corresponding to the maximum angle β_0, is fixed by the plane tangential to the neighboring C_y. Hence β_0 is determined by

$$1-\cos\beta_0 = (\Delta K/k_F)\tan\chi, \tag{19}$$

where $\Delta K = K - k_F$. Integrating over all the orbits covering the wedge and using Eq. 4, we obtain the conductivity σ^{loop}

$$\sigma^{loop}(\chi) = n^{(1)}e\mu\frac{k_F}{K-2k_F}\,\mathcal{G}(\chi), \tag{20}$$

where $\mathcal{G}(\chi)$ is the dimensionless integral

$$\mathcal{G}(\chi) = \frac{2}{\pi}\frac{e^{-\alpha\pi/2}}{(1-e^{-2\pi\alpha})}\frac{\alpha\cot\chi}{(1+\alpha^2)}\int_0^{\beta_0}(\beta-\frac{1}{2}\sin 2\beta)\times \\ [\alpha\sin\beta\cosh\alpha\beta - \cos\beta\sinh\alpha\beta]\sin\beta\, d\beta. \tag{21}$$

$\mathcal{G}(\chi)$ is plotted in Fig. S1. As shown, σ^{loop} is strongly suppressed. Even when $\chi \to \gamma_c$ (all states on C_y are open orbits), σ^{loop} is $< 0.015\times\sigma^{(1)}$. The suppression accounts for the observed increase in ρ_{xx} when $\mathbf{B}$ is tilted away from $\hat{\mathbf{z}}$ in the TAMR experiment.

[1] T. Liang, Q. Gibson, M. N. Liu, R. J. Cava and N. P. Ong, Ultrahigh mobility and giant magnetoresistance in the Dirac semimetal Cd_3As_2, *Nat. Mater.* **14**, 280-284 (2015).

[2] M. N. Ali, J. Xiong, S. Flynn, J. Tao, Q. D. Gibson, L.M. Schoop, T. Liang, N. Haldolarachchige, M. Hirschberger, N. P. Ong and R. J. Cava, Large, non-saturating magnetoresistance in WTe_2, *Nature* **514**, 205-208 (2014).

[3] C. W. Hicks, A. S. Gibbs, A. P. Mackenzie, H. Takatsu, Y. Maeno, and E. A. Yelland, Quantum Oscillations and High Carrier Mobility in the Delafossite $PdCoO_2$, *Phys. Rev. Lett.* **109**, 116401 (2012). DOI: 10.1103/PhysRevLett.109.116401

[4] P. Kushwaha *et. al.*, Nearly-free electrons in a 5d delafossite oxide metal, *Science Advances* **1**, 1-7 (2015). DOI: 10.1126/sciadv.1500692

[5] N. Nandi *et al.*, Unconventional magneto-transport in ultrapure $PdCoO_2$ and $PtCoO_2$, *NPJ Quant. Mat.* **3**, 66 (2018).

[6] J. C. A. Prentice and A. I. Coldea, Modeling the angle-dependent magnetoresistance oscillations of Fermi surfaces with hexagonal symmetry, *Phys. Rev. B* **93**, 245105 (2016). DOI: 10.1103/PhysRevB.93.245105

[7] N. J. Ghimire, M. A. Khan, A. S. Botana, J. S. Jiang, and J. F. Mitchell, Anisotropic angular magnetoresistance and Fermi surface topology of the candidate novel topological metal Pd_3Pb, *Phys. Rev. Mater.* **2**, 081201(R) (2018). DOI: 10.1103/PhysRevMaterials.2.081201

[8] C. Bergemann, S. R. Julian, A. P. Mackenzie, S. Nishizaki, and Y. Maeno, Detailed Topography of the

Fermi Surface of Sr_2RuO_4, *Phys. Rev. Lett.* **84**, 2662-2665 (2000). DOI: 10.1103/PhysRevLett.84.2662

[9] K. Yamaji, On the angle dependence of the magnetoresistance in quasi-two-dimensional organic superconductors, *J. Phys. Soc. Jpn.* **58**, 1520-1523 (1989).

[10] R. Yagi, Y. Iye, T. Osada and S. Kagoshima, Semiclassical interpretation of the angular-dependent oscillatory magnetoresistance in quasi-two-dimensional systems, *J. Phys. Soc. Jpn.* **59**, 3069-3072 (1990).

[11] T. Suzuki, L. Savary, J.-P. Liu, J. W. Lynn, L. Balents, J. G. Checkelsky, Singular angular magnetoresistance in a magnetic nodal semimetal, *Science* **365**, 377-381 (2019). 10.1126/science.aat0348

[12] L. F. Matthiess, Band structure and Fermi surface of ReO_3, *Phys. Rev.* **181**, 987 (1969).

[13] F. Cora, M. G. Stachiotti, and C. R. A. Catlow, Transition Metal Oxide Chemistry. Electronic Structure Study of WO_3, ReO_3, and $NaWO_3$, *J. Phys. Chem. B* **101**, 3945-3952 (1997).

[14] M. G. Stachiotti, F. Cora, C. R. A. Catlow and C. O. Rodriguez, First-principles investigation of ReO_3 and related oxides, *Phys. Rev. B* **55** 7508-7514 (1997).

[15] J. E. Graebner and E.S. Greiner, Magnetothermal oscillations and the Fermi Surface of ReO_3, *Phys. Rev.* **185**, 992 (1969).

[16] S. M. Marcus, Measurement of the de Haas van Alphen effect in the transition metal oxide ReO_3, *Phys. Lett.* **27A**, 584-585 (1968).

[17] R. A. Phillips and H. R. Shanks, de Haas van Alphen effect in ReO_3, *Phys. Rev. B* **4**, 4601 (1971).

[18] F. S. Razavi and W. R. Datars, Cyclotron masses in ReO_3 measured by the de Haas van Alphen effect, *Can. J. Phys.* **54**, 845 (1976).

[19] T. P. Pearsall and C. A. Lee, Electronic transport in ReO_3: DC conductivity and Hall effect, *Phys. Rev. B* **10**, 2190 (1974).

[20] J. Falke *et. al.*, Electronic structure of the metallic oxide ReO_3, *Phys. Rev. B* **103**, 115125 (2021). DOI: 10.1103/PhysRevB.103.115125

[21] E. H. Lieb, Two theorems on the Hubbard model, *Phys. Rev. Lett.* **62**, 1201 1204 (1989). DOI: 10.1103/PhysRevLett.62.1201

[22] Z. Liu, F. Liu and Y.-S. Wu, Exotic electronic states in the world of flat bands: From theory to material, *Chin. Phys. B* **23**, 077308 (2014). DOI: 10.1088/1674-1056/23/7/077308

[23] N. Regnault *et al.*, Catalogue of Flat Band Stoichiometric Materials, cond-mat arXiv: 2106.05287.

[24] *Principles of the Theory of Solids*, J. M. Ziman (Cambridge Univ. Press 1972), Ch. 9.

Acknowledgement We have benefitted from discussions with E. Lieb, B. A. Bernevig and N. Regnault. RJC and NPO acknowledge support by the U.S. National Science Foundation under award DMR 2011750.

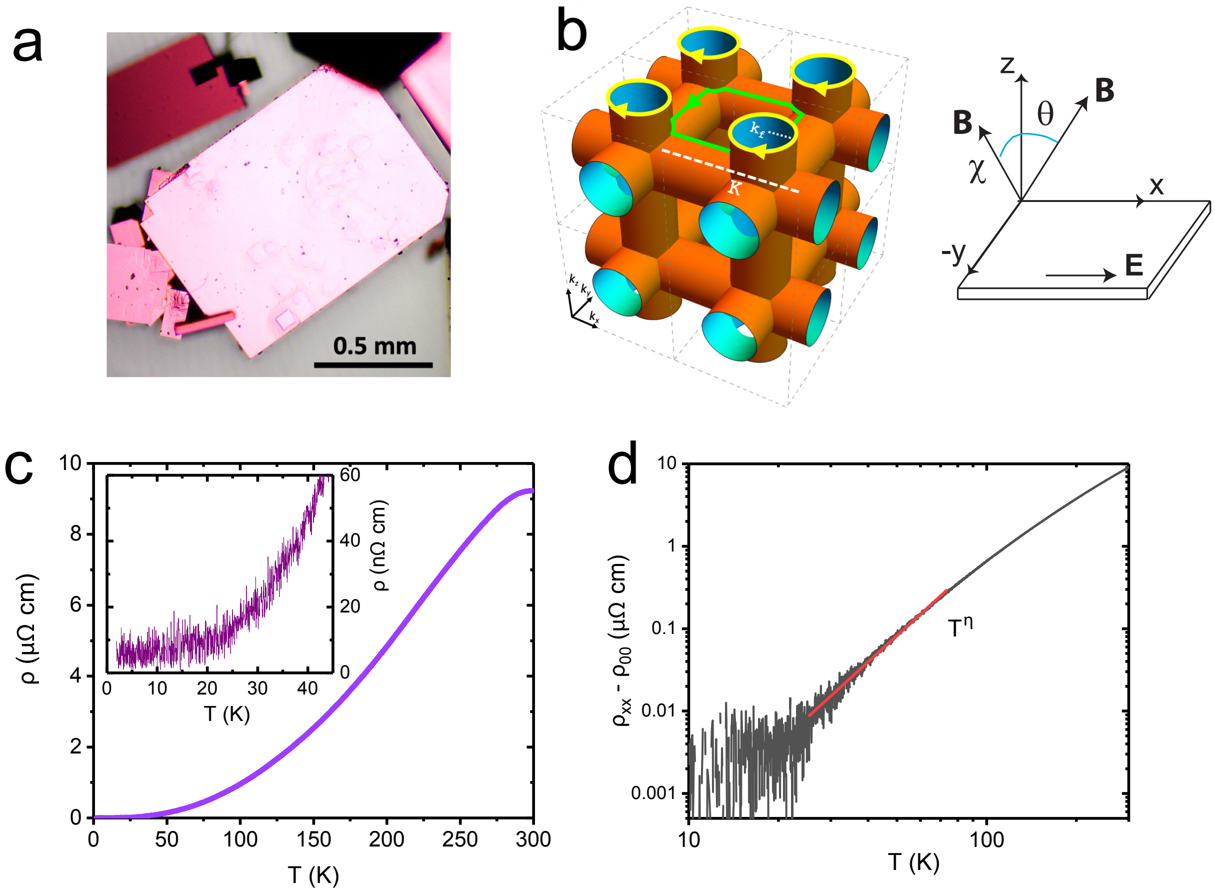

FIG. 1. (a) Crystals of ReO_3 showing characteristic brilliant pink hue in reflected light. The cubic cell parameter a is 3.748 Å. (b) Sketch of the jungle-gym FS sheet in extended zone scheme with 8 Brillouin zones (BZ) shown. The reciprocal lattice vector $K = 2\pi/a$ denotes the size of the cubic BZ and $k_f = 0.23$K is the cylinder radius. With $\mathbf{B} \parallel \mathbf{z}$, closed cyclotron orbits form around the cross-sections of the FS in the $k_x - k_y$ plane. At different k_z, the orbits change from closed and electron-like (4 yellow loops) to closed and hole-like (green loop). The inset shows the field tilt-angles θ and χ relative to axes (x, y, z). (c) Plot of the resistivity ρ vs. T with $B = 0$. The residual value ρ_{00}, measured in 4 crystals, is 5-8 nΩcm (inset). (d) Log-log plot of $\Delta\rho$ vs. T where $\Delta\rho(T) = \rho(T) - \rho_{00}$. A linear fit (red line) over $20 < T < 80$ K gives $\Delta\rho = T^\eta$ with $\eta = 3.1 \pm 0.2$.

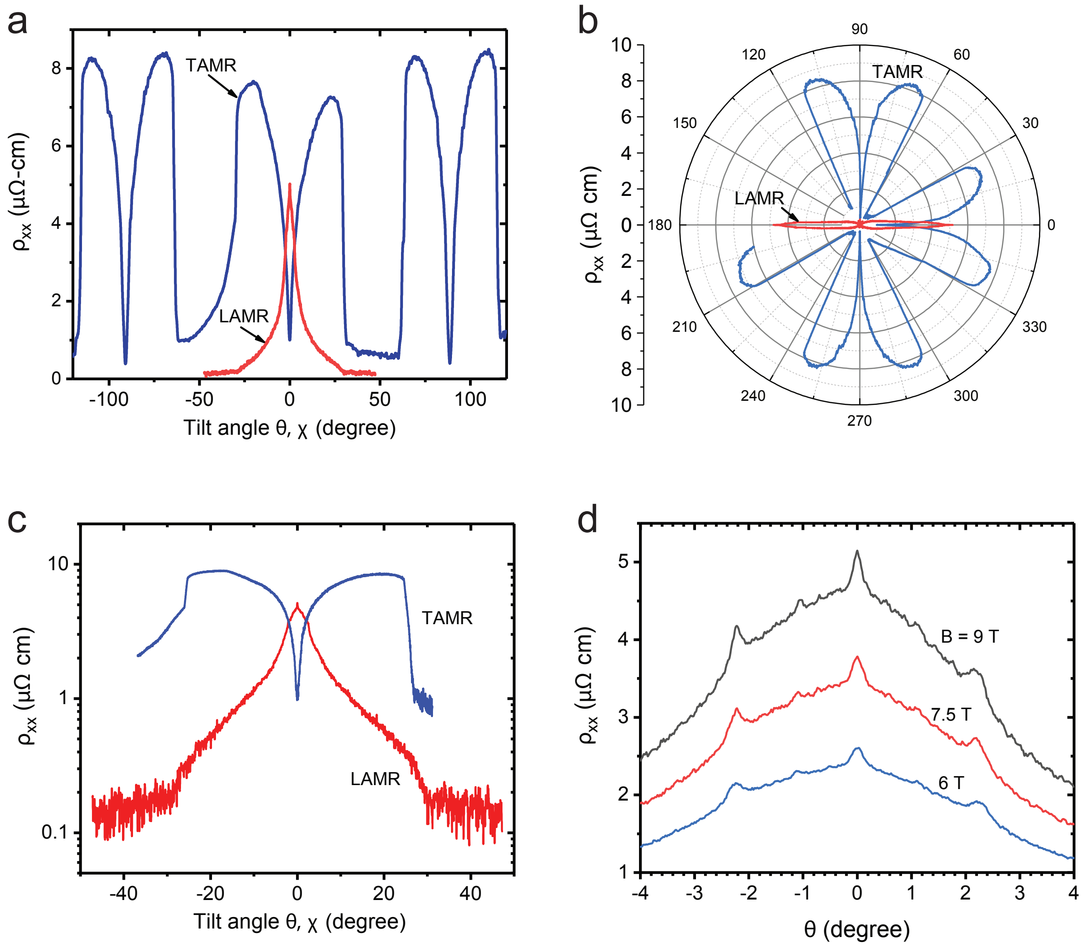

FIG. 2. Panel (a): The singular, anisotropic angular magnetoresistance $\rho_{xx}(\theta, \chi)$ measured at $T = 1.9$ K with $\mathbf{E} \parallel \hat{\mathbf{x}}$ and $|\mathbf{B}|$ fixed at 9 T. The LAMR curve (in red) plots $\rho_{xx}(\theta, 0)$ vs. θ with $\mathbf{B}$ lying in the (longitudinal) x-z plane at angle $\theta = \angle(\mathbf{B}, \hat{\mathbf{z}})$. The TAMR curve (blue) plots $\rho(0, \chi)$ vs. χ with $\mathbf{B}$ in the transverse y-z plane at angle $\chi = \angle(\mathbf{B}, \hat{\mathbf{z}})$. A slight misalignment causes a weak breaking of mirror symmetry about $\chi = 0$ or $\theta = 0$ (see text). The singular AMR complicates determination of $\rho_{xx}(\theta, \chi)$ at $(\theta, \chi) = (0, 0)$. Panel (b) shows the polar plot of the TAMR and LAMR curves. The TAMR curve (blue) displays C_4 symmetry. However, the LAMR curve (red) exhibits C_2 symmetry because, with $\mathbf{E}$ fixed $\parallel \hat{\mathbf{x}}$, $\rho_{xx}(0, 0) \gg \rho_{xx}(\pi/2, 0)$ (the latter is equal to $\rho_{zz}(0, 0)$). Panel (c) is an expanded view of the curves of LAMR (red) and TAMR (blue) in semi-log plot. The TAMR curve shows a steep decrease at the completion angle γ_c. The step decrease in the LAMR curve is milder but still well resolved. Panel (a): Expanded view of the LAMR curve $\rho_{xx}(\theta, 0)$ at 1.9 K with $|\mathbf{B}|$ fixed at 6 T (blue curve), 7.5 T (red) and 9 T (grey). In all three curves, sharp resonant features are observed at $\theta = 0$, $\pm 1.1°$ and $\pm 2.2°$.

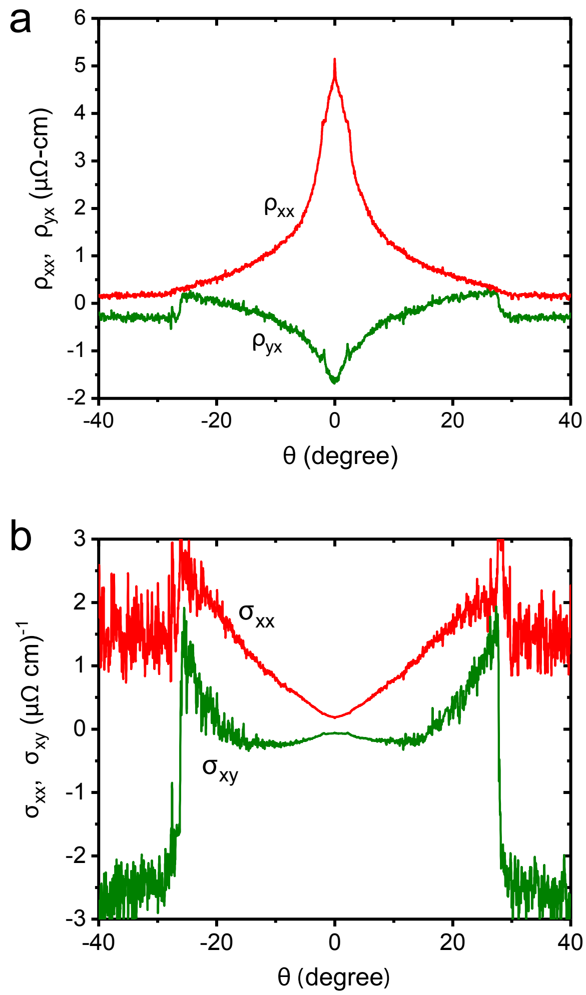

FIG. 3. Panel (a): Comparison of the angular Hall resistivity $\rho_{yx}(\theta, 0)$ (green curve) and $\rho_{xx}(\theta, 0)$ (red curve) measured vs. θ (setting $\chi = 0$) at 1.9 K with $|\mathbf{B}|$ fixed at 9 T. Initially, ρ_{yx} is electron-type at $\theta = 0$, but changes to hole-like near 16°. At γ_c, ρ_{yx} undergoes a step-wise change, involving a second sign-change. The curves for the inferred conductivity σ_{xx} (red curve) and Hall conductivity σ_{xy} (green) are plotted in Panel (b). At small θ, σ_{xy} is negative. Near 16°, it changes sign and increases steeply before suffering a large discontinuous jump at γ_c to return to negative values.

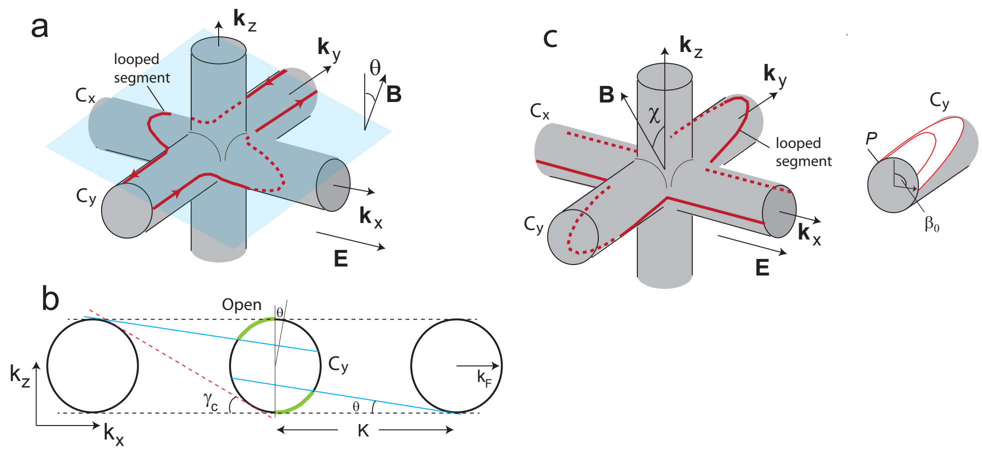

FIG. 4. Sketch of open orbits. Panel (a) shows the three FS cylinders C_x, C_y and C_z (grey tubes) and a plane normal to $\mathbf{B}$ (pale blue). Intersections of the FS with the normal planes define possible orbits of a wave packet. In the LAMR experiment, when $\mathbf{B}$ is tilted by θ relative to $\hat{\mathbf{z}}$, an open orbit can emerge (thick curves). A right-moving wave packet on C_y loops under C_x (dashed curve) before resuming its orbit on C_y. The left-moving partner loops over C_x. In the high-B limit, these open orbits contribute strongly to σ_{xx}. Panel (b) shows end-on views of 3 cylinders C_y in the repeated zone scheme with $K = 2\pi/a$. The planes normal to $\mathbf{B}$ that are tangential to the outer cylinders (blue lines) define the FS portion hosting open orbits on the middle cylinder (thick green arcs). States outside the green arcs remain in closed orbits. The green arcs lengthen rapidly as $\theta \to \gamma_c$, the completion angle defined by the inner tangent (red dashed line). Panel (c): Sketch of open orbits in the TAMR experiment. With $\mathbf{B}$ tilted by angle χ relative to $\hat{\mathbf{z}}$ in the plane transverse to $\mathbf{E}$, the open orbits are straight-line segments on C_x alternating with looped segments on C_y. The inset on the right shows the conical wedge (white area) on C_y. Cyclotron orbits on the wedge (red ellipses) project onto circular orbits $\mathcal{P}$ on the cross-section (front end-face of C_y). Each orbit subtends an angle 2β on $\mathcal{P}$, while the longest one subtends angle $2\beta_0$. The conductivity arising from states on the entire wedge is obtained by integrating the orbits over the white area (Eq. 21).

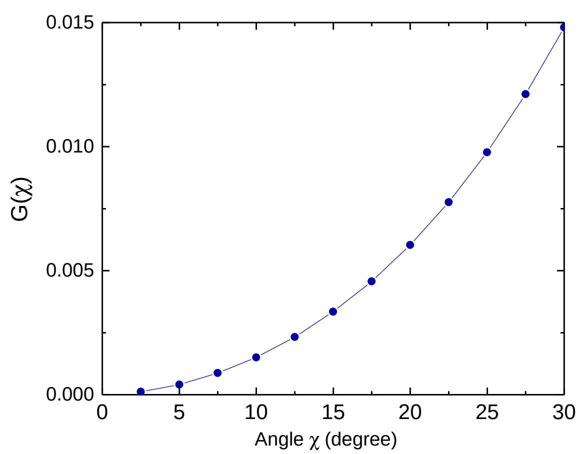

FIG. S1. Variation of the dimensionless integral $\mathcal{G}$ (Eq. 21) vs. tilt angle χ. Even when $\chi \to \gamma_c$, $\mathcal{G}$ is <0.015. This implies that the when all the states on C_y are converted to open orbits, its conductivity is suppressed to less than 1.5% of the value at $\chi = 0$ (see Eq. 20).

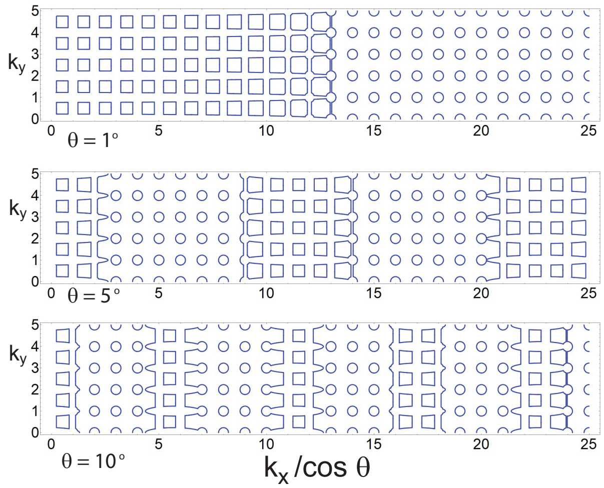

FIG. S2. Numerical simulation of the pattern of open and closed orbits at three selected values of θ $(1^\circ, 5^\circ, 10^\circ)$ with $\chi = 0$ in the LAMR experiment. The cross-section displayed is centered on the intersection of the cylinders. The array extends over 25 Brillouin Zones in the extended zone scheme. The orbits lie in a plane normal to $\mathbf{B}$ with the horizontal axis $k_x/\cos\theta$ measured in the direction $\hat{\mathbf{z}} \times \mathbf{B}$. In each panel, the orbits are quasiperiodic despite the appearance of nominal periodicity.

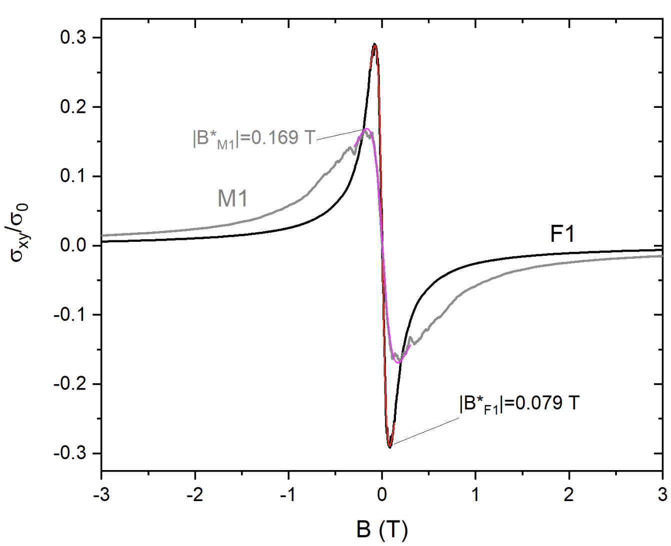

FIG. S3. Plot of the Hall conductivity σ_{xy}/σ_0 vs. B at 2 K and zero tilt angle. The low-field dependence was fit to a semiclassical model; peaks in σ_{xy}(B) occur at $|\mu B^*| = 1$. For two different samples this yielded μ = 59,000 cm^2/Vs (M1) and 126,000 cm^2/Vs (F1).